Catalyst design by scanning probe block copolymer lithography

Liliang Huang[a,1], Peng-Cheng Chen[a,b,1], Mohan Liu[a], Xianbiao Fu[b,c,d], Pavlo Gordiichuk[b,e], Yanan Yu[c], Chris Wolverton[a], Yijin Kang[b,c,d,2], and Chad A. Mirkin[a,b,e,2]

[a]Department of Materials Science and Engineering, Northwestern University, Evanston, IL 60208; [b]International Institute for Nanotechnology, Northwestern University, Evanston, IL 60208; [c]Institute of Fundamental and Frontier Sciences, University of Electronic Science and Technology of China, 610054 Chengdu, China; [d]University of Electronic Science and Technology of China–Northwestern University Joint Center for Materials Research, Northwestern University, Evanston, IL 60208; and [e]Department of Chemistry, Northwestern University, Evanston, IL 60208

Contributed by Chad A. Mirkin, February 14, 2018 (sent for review January 18, 2018; reviewed by Thomas E. Mallouk and Younan Xia)

Scanning probe block copolymer lithography (SPBCL), in combination with density-functional theory (DFT), has been used to design and synthesize hydrogen evolution catalysts. DFT was used to calculate the hydrogen adsorption energy on a series of single-element, bimetallic, and trimetallic (Au, Pt, Ni, and Cu) substrates to provide leads that could be synthesized in the form of alloy or phase-separated particles via SPBCL. PtAuCu (18 nm, ∼1:1:1 stoichiometry) has been identified as a homogeneous alloy phase that behaves as an effective hydrogen evolution catalyst in acidic aqueous media, even when it is made in bulk form via solution phase methods. Significantly, the bulk-prepared PtAuCu/C nanocatalyst discovered via this process exhibits an activity seven times higher than that of the state-of-the-art commercial Pt/C catalyst (based upon Pt content). The advantage of using SPBCL in the discovery process is that one can uniformly make particles, each consisting of a uniform phase combination (e.g., all alloy or all phase-segregated species) at a fixed elemental ratio, an important consideration when working with polyelemental species where multiple phases may exist.

lithography | hydrogen evolution reaction | multimetallic nanocatalyst | catalysis

Catalyst design and optimization is extremely challenging, especially when nanoparticles are the active structures. In addition to composition, the size, shape, and surface structure are important considerations (1–21). For polyelemental systems, the design challenges are substantially greater since the configurational complexity in these alloy systems adds significant new degrees of freedom to structure–function relationships. For example, the alloying and phase-segregating behavior of polyelemental systems can lead to new and unexpected catalytic properties (12). This observation presents several significant challenges. First, with many solution-based synthesis protocols, it is difficult, if not impossible, to control "phase purity" in multimetallic nanoparticle systems, since many potentially catalytically active structures are kinetic rather than thermodynamic products. Second, when one considers particle size, composition, shape, and degree of alloying or phase segregation, the sheer number of possibilities is daunting. To address this challenge, ways of making polyelemental particles and controlling their state of alloying or phase segregation combined with methods for screening them and reducing the numbers that need to be produced at scale to validate properties of interest must be developed. This requires a combinatorial approach, the use of theory to minimize targets of opportunity, or a combination of both. Herein, we use an emerging nanoparticle synthetic tool called scanning probe block copolymer lithography (SPBCL) and density-functional theory (DFT) to explore three-component particles consisting of combinations of Pt, Au, Cu, and Ni. This is an excellent proof-of-concept system to evaluate the utility of such an approach since Pt is known to be the best single-element catalyst for the hydrogen evolution reaction (HER), and additional elements can be used to tune the H-adsorption properties of the multimetallic systems (22).

In this work, we selected the HER as a proof-of-concept due to its importance in the commercial production of H_2 (23–25). In an acidic electrolyte, the catalyst's hydrogen binding energy (HBE) is the sole reaction descriptor for the HER (22, 23, 26). According to the Sabatier principle, an optimal HER catalyst should have an HBE that is neither too strong (e.g., strong adsorbing surface: W, Mo, Fe, Co, Ni, etc.) nor too weak (e.g., weak adsorbing surface: Au, Ag, Cu, etc.) (22). Pt is the best single-element catalyst for the HER, but in principle could be further improved if its HBE was reduced (22). Electronically tuning the *d*-band electronic structure of Pt by alloying it with other elements has proven to be an effective way of tailoring its adsorption properties (27–31). Indeed, alloying Au with Pt reduces the HBE and increases the nobility of the catalyst, thereby enhancing its stability (30, 32–34). Adding a third metal into the Pt–Au system may further improve the HBE by providing an

Significance

It is a major challenge in catalysis to uncover structure–performance relationships that drive the design and optimization of high-performance/low-cost catalysts. When one considers the number of potential elemental combinations for catalysts and then includes variables, such as particle size and elemental stoichiometry, the number of possibilities is daunting. There are also significant challenges facing the synthetic chemist, who is tasked with making and characterizing such complex architectures. Indeed, a way of substantially narrowing the field is essential. In this work, we introduce an effective approach that combines computational prediction, experimental verification using a well-defined nanomodel, and finally production of high-performance catalysts in bulk as a powerful tool for discovering and designing catalysts for energy conversion and storage.

Author contributions: L.H., P.-C.C., Y.K., and C.A.M. designed the experiments; M.L. and C.W. performed DFT studies; Y.K. and C.A.M. conceived and supervised the project; L.H., Y.K., and C.A.M. analyzed results; L.H. carried out the experiments (synthesis, characterization, and HER evaluation) on SPBCL; X.F. and Y.Y. synthesized nanoparticles in solution phase and evaluated their HER performance; L.H., P.-C.C., M.L., X.F., P.G., Y.Y., C.W., Y.K., and C.A.M. discussed the results; and L.H., P.-C.C., M.L., X.F., P.G., Y.Y., C.W., Y.K., and C.A.M. wrote the paper.

Reviewers: T.E.M., The Pennsylvania State University; and Y.X., Georgia Institute of Technology.

Conflict of interest statement: C.M. and Y.X. are coauthors on a review article published in 2015.

[1]L.H. and P.-C.C. contributed equally to this work.

[2]To whom correspondence may be addressed. Email: kangyijin@uestc.edu.cn or chadnano@northwestern.edu.

This article contains supporting information online at www.pnas.org/lookup/suppl/doi:10.1073/pnas.1800884115/-/DCSupplemental.

Published online March 23, 2018.

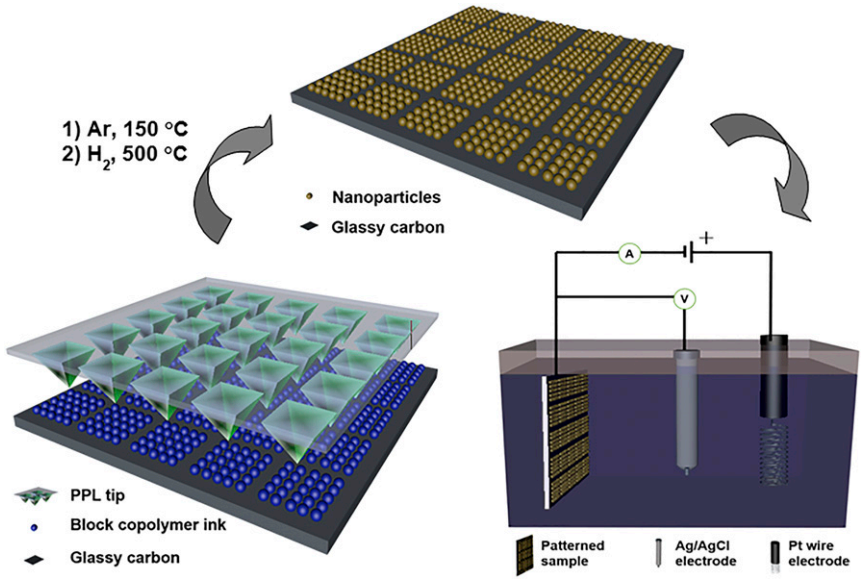

Fig. 1. Process for synthesizing nanoparticles by SPBCL and then studying their HER catalytic properties. (*i*) PPL is used to pattern PEO-*b*-P2VP nanoreactors, loaded with the appropriate metal salts, onto a glassy carbon substrate. Each nanoreactor has a near-identical volume and contains approximately the same number and type of atoms. (*ii*) The metal ion contents of the nanoreactors are thermally transformed into nanoparticles under a reducing environment. (*iii*) The patterned substrate is then used as a working electrode in a three-electrode cell to study HER catalysis. A, current reading; V, voltage.

additional variable for fine-tuning adsorption energy. The addition of a third element provides access to many structures, defined not only by stoichiometry but also by phase (alloyed or phase-segregated). To test this hypothesis and identify the most active HER catalysts, we investigated the PtAu–M (M = Ni, Cu) trimetallic system. We first used DFT calculations to evaluate the HBE for potential target particle structures, and then synthesized them and evaluated their catalytic properties. Importantly, SPBCL allows one to synthesize particles that are uniform both in terms of stoichiometry and phase. Through this exercise, we identified PtAuCu as having the optimal calculated HBE (based upon a volcano plot) and correspondingly, the highest measured HER activity.

Results and Discussion

Preparation of Uniform Model Catalysts. SPBCL confines metal precursors within individual polymer nanoreactors. Each nanoparticle grows by consuming the precursors within the polymer reactor, isolated from the growth of other nanoparticles (35–37). Therefore, the uniformity of nanoparticles in terms of size, phase structure, and composition can be exquisitely controlled (35–37). In a typical experiment (Fig. 1), the patterning ink is prepared by mixing the aqueous block copolymer solution poly(ethylene oxide)-*block*-poly(2-vinylpyridine) (PEO-*b*-P2VP) with metal precursors (salts), followed by spin-coating onto the polymer pen lithography (PPL) tips (38). The PPL tips are then brought into contact with a glassy carbon substrate to make predesigned arrays of homogeneous nanoreactor domes (Fig. 2 *A*–*C*). Here, glassy carbon is used because it is a catalytically inert substrate (6, 33) and compatible with the SPBCL process. After the patterning process, the substrate is transferred into a tube furnace for a two-step thermal annealing procedure, where the metal precursors are aggregated and reduced. Throughout the SPBCL process, PEO-*b*-P2VP serves three functions: (*i*) to load the metal precursors, effectively acting as a solvent, (*ii*) to facilitate the delivery of the patterning ink from tip to surface, and (*iii*) to confine the nucleation and aggregation process within a small well-defined volume and direct the formation of single nanoparticles. Only one nanoparticle per nanoreactor typically forms (Fig. 2*D*).

Pt, Au, Ni, and Cu were selected to verify the effectiveness of SPBCL as a catalyst screening and design platform, because they are common components of HER catalysts. Transmission electron microscopy (TEM), high-angle annular dark field scanning transmission electron microscopy (HAADF-STEM), and energy-dispersive X-ray spectroscopy (EDS) were employed to characterize SPBCL-produced nanoparticles (Fig. 3 and *SI Appendix*, Fig. S1). The nanoparticle sizes are controlled in the 15–20-nm range by tuning the nanoreactor volume and metal loading; particles less than 20 nm in diameter are typically used as HER catalysts (6, 33, 34, 39). Monometallic nanoparticles are synthesized using water-soluble $H_2PtCl_6{\cdot}6H_2O$, $HAuCl_4{\cdot}3H_2O$, $Cu(NO_3)_2{\cdot}3H_2O$, and $Ni(NO_3)_2{\cdot}6H_2O$ as precursors in the SPBCL

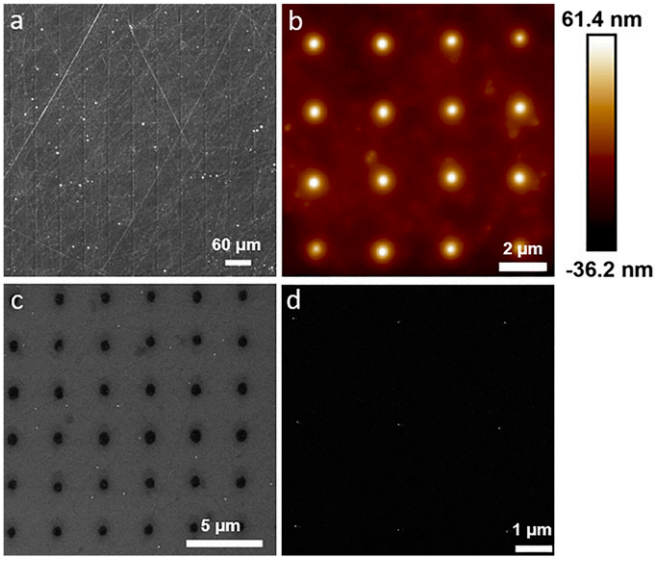

Fig. 2. (*A*) Dark-field optical microscopy image, (*B*) AFM topographical image, and (*C*) SEM image of uniformly patterned nanoreactor arrays by SPBCL. (*D*) SEM image of an array of PtAuCu trimetallic nanoparticles on glassy carbon.

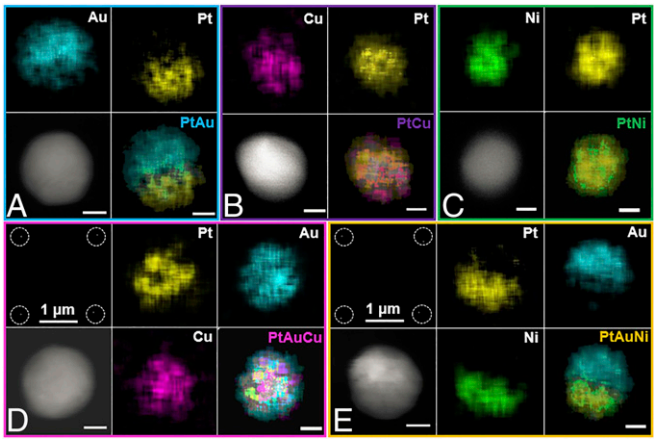

Fig. 3. HAADF-STEM images and EDS maps of multimetallic nanoparticles synthesized by SPBCL: (*A*) PtAu, (*B*) PtCu, (*C*) PtNi, (*D*) PtAuCu, and (*E*) PtAuNi. Representative HAADF-STEM images of arrays of 2 × 2 nanoparticle arrays are shown in *D* and *E*. Dotted circles are used to highlight the position of the nanoparticles as a guide to the eye. Only one nanoparticle is observed at each site. (Scale bars: 5 nm unless otherwise noted.)

process. The average stoichiometry of the final product is almost identical to the ratio of starting materials, due to the nanoreactor's ability to confine and direct the reaction toward single-nanoparticle growth (*SI Appendix*, Table S1). Among the Pt–M (M = Au, Cu, Ni and Pt:M = 1:1) binary nanoparticles, PtCu and PtNi form homogeneous alloy phases since Cu and Ni are miscible with Pt, while PtAu is defined by a phase-segregated heterostructure that forms when the Au content is 50%, a result supported by theory (40, 41). At a 1:1:1 Pt:Au:M (M = Ni, Cu) ratio, PtAuCu exhibits a homogeneous alloy phase, while PtAuNi forms a phase-segregated heterostructure in which Pt and Ni are miscible, but Au is immiscible with the other two metals in the particle (Fig. 3). Notably, regardless of phase (homogeneous alloy phase or phase-segregated), all SPBCL synthesized nanoparticles exhibit only one general type of phase combination under the conditions studied. Such high phase purity in multielemental particles is not easily realizable via conventional synthetic methods since it is challenging to synchronize the reduction of all metal ions in a precursor solution and to control site-selective nucleation (42). In addition, it is difficult to isolate nucleation events from the growth stage, and therefore difficult to prevent the formation of complex product mixtures. Indeed, in an attempt to prepare PtAuNi ternary nanoparticles via the most popular solution-phase synthesis in one pot, we obtained a mixture of *fcc* Au and Pt-based A1 alloy phases (*SI Appendix*, Fig. S2). In contrast, the SPBCL approach renders a high degree of both size control and phase purity of nanoparticles (Fig. 3). Such high uniformity is attractive for catalyst screening and design because it allows for the correlation between catalytic properties and the chemical/physical properties of the catalysts.

Computational Prediction of PtAuM Trimetallic Catalyst. HER catalyst design has been well-established via the concept of volcano plots, which rationalize catalyst performance by connecting it to optimal adsorption properties (31, 43). Pt is widely accepted as the most active monometallic catalyst toward the HER, since it is the element that is closest to the peak position of the volcano plot (31, 43). Fe, Co, and Ni result in strong hydrogen adsorption while Au, Ag, and Cu exhibit weaker interactions with hydrogen (17, 33). Therefore, none of them has comparable HER activity to Pt. However, adding a second or even third metal into Pt has proven to be a viable approach for tailoring the adsorption properties of Pt to reach the Sabatier optimum (43). Using DFT (44–47), we examine the HBE, the sole descriptor of HER in an acidic environment, on the (111) surface of monometallic, bimetallic, and trimetallic catalysts (*SI Appendix*, Fig. S3 and Tables S2 and S3). Our computational results of monometallic catalysts are consistent with previous reports (31, 43): Ni (−0.492 eV), which adsorbs hydrogen strongly, is located on the left half of the volcano plot, Pt (−0.410 eV) occupies a position that is slightly left to the peak of the volcano, while Cu (−0.172 eV) and Au (0.224 eV), with low HBE (or even positive, unfavorable), are positioned on the right half of the plot. In the bimetallic system, in contrast with Vegard's law for the determination of alloy lattice parameters (48), the HBE of a bimetallic alloy is not necessarily the average of its two components. For instance, PtCu has an HBE of −0.450 eV, which is even stronger than that of pure Pt, even though Cu itself weakly adsorbs hydrogen. While Pt–M bimetallic catalysts exhibit great tunability in their adsorption properties, they are nevertheless unable to reach the peak of the volcano plot. However, we find that the Pt–Au–M trimetallic system offers an additional factor for the fine-tuning of adsorption strength. Moreover, as the most noble metal, Au is expected to enhance the overall chemical stability of the trimetallic catalysts. The trimetallic system also helps to further reduce the Pt content, over a pure Pt catalyst. PtAuNi (−0.368 eV) and PtAuCu (−0.326 eV), with a homogeneous alloy phase, are identified as the optimal hydrogen adsorbents.

Experimental Verification with Nanoparticle Array Model Catalysts. Because of their high uniformity, SPBCL-synthesized nanoparticle arrays are ideal model catalysts. Therefore, Pt, PtAu, PtCu, PtNi, PtAuNi, and PtAuCu nanoparticle arrays were used to experimentally evaluate the prediction made by DFT (see *SI Appendix* for details). HER catalyst particles were tested with a three-electrode setup in which a glassy carbon disk with nanoparticle arrays was used as the working electrode, Ag/AgCl as the reference electrode, and a coiled Pt wire as the counter electrode. Au wire was also used as a counter electrode to avoid complications from possible redeposition of Pt onto the working electrode during the test cycles. PtAuCu exhibits the lowest overpotential among the listed multimetallic catalysts (Fig. 4 *A* and *B*), consistent with the DFT prediction. When the current density is normalized to the content of Pt in each catalyst, at an overpotential of 0.4 V, PtAuCu shows a current density of 37.4 mA cm^{-2}, that is more than three times the current density obtained with Pt (12.3 mA cm^{-2}) (Fig. 4*C*). However, PtAuNi only exhibits a current density of 9.85 mA cm^{-2}, contrary to the DFT prediction. In the volcano plot (Fig. 4*D*), the PtAuNi alloy occupies the position close to the peak, denoted as PtAuNi*. Surprisingly, the actual exchange-current density measured for SPBCL-synthesized PtAuNi is up to two orders of magnitude lower than the DFT predicted value. A closer inspection of the particles synthesized by SPBCL provides a clue to this discrepancy. Indeed, the DFT prediction is based on a PtAuNi homogeneous alloy, and while PtNi can form a homogeneous alloy, Au is immiscible with Pt or Ni, at a 1:1 ratio. Importantly, the EDS characterization of the trimetallic PtAuNi particle shows that it is a PtNi–Au heterostructure as opposed to a three-element alloy. This observation underscores one of the major beneficial attributes of studying catalyst particles synthesized by SPBCL. The high uniformity of these structures allows one to identify and study key structural features that are often missed in idealized and simplified computational approaches.

With this understanding in hand, we set up a computational model to mimic the observed PtNi–Au heterostructure (*SI Appendix*, Fig. S4). The surface of PtNi–Au is divided into four compositional regions: (1) Au–Ni, (2) Au, (3) Au–Pt, and (4) Pt–Ni. In each region, adsorbed hydrogen atoms bind with either one or two types of metal. We consider all of the unique *fcc* and *hcp* adsorption sites in each region, with adsorption coverage of 1/12 of a monolayer (ML). The computational results show

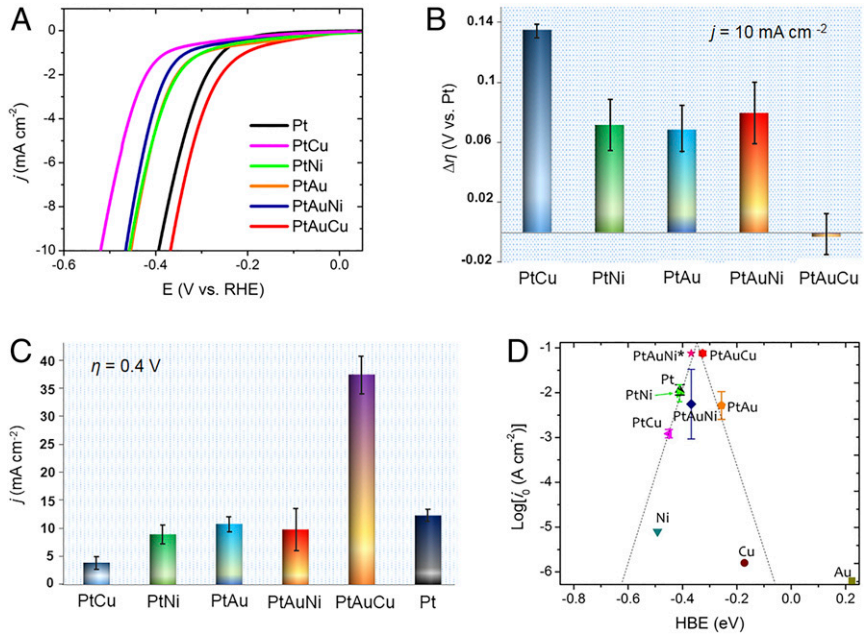

Fig. 4. (*A*) Representative HER polarization curves and statistical results from all HER measurements showing (*B*) the overpotential difference at 10 mA cm^{-2} of various SPBCL-synthesized multimetallic nanoparticle catalysts (the overpotential of SPBCL-synthesized Pt is used as a comparison), and (*C*) current densities at the overpotential of 0.4 V (the current densities are normalized to the content of Pt in each particle). (*D*) A volcano plot, in which the exchange current densities are calculated from Tafel plots and the HBE values are calculated by DFT. Error bars represent the standard deviation.

that hydrogen adsorption near an interface is weaker than that on a uniform PtNi alloy surface (*SI Appendix*, Fig. S4*B*), indicating that an interfacial effect indeed influences the HBE of PtNi even though Au atoms are not directly in contact with the hydrogen atoms. Under the influence of interfacial Au, Pt–Ni in region 4 exhibits the optimal HBE (−0.325 eV). In contrast, the HBEs on the sites in the three other regions are substantially weaker than the optimum value: −0.056 eV for Au–Ni in region 1, 0.092 eV in region 2, and −0.257 eV for Pt–Au in region 3. Therefore, compared with alloy-phase PtAuNi, phase-segregated PtNi–Au has fewer desired sites, which leads to significantly lower activity. Here, it is emphasized that in addition to size, shape, and composition, the phases of catalyst materials may be crucial for realizing desirable catalytic activity. Due to the unique phase purity rendered by SPBCL synthesis, we can unambiguously attribute the reduced HER activity to the phase segregation of PtAuNi. To the best of our knowledge, despite desirable HER activity, alloy-phase PtAuNi is not easily prepared by any conventional synthetic methods. Taken together, one can conclude that phase-segregated PtAuNi materials have limited value in HER.

In contrast, for the PtAuCu trimetallic system, although Pt and Au have poor miscibility, Cu is miscible with both Au and Pt. Therefore, PtAuCu can form a homogeneous trimetallic alloy (Fig. 3), allowing one to electronically modify Pt with contributions from both Cu and Au. Hence, experimentally, such particles exhibit the highest current densities (Fig. 4).

Design of Nanostructured PtAuCu as High-Performance HER Catalyst. Although the DFT predictions and SPBCL model catalyst studies provide guidance with regard to optimum composition and structure for an HER catalyst, for them to be practically useful, catalysts in bulk amounts which exhibit comparable properties must be attainable. Therefore, we explored the behavior of PtAuCu nanoparticles synthesized via a solution phase method. Platinum acetylacetonate, gold chloride, and copper acetylacetonate were coreduced in the presence of oleylamine and oleic acid at 230 °C, a common method for trimetallic nanoparticle synthesis (33, 34, 49). The as-synthesized nanoparticles have a diameter of 12 nm and a composition of PtAuCu (Fig. 5*A* and *SI Appendix*, Fig. S5). EDS mapping experiments show that Pt, Au, and Cu are homogeneously distributed throughout the as-synthesized particles (Fig. 5*B*). Inductively coupled plasma mass spectrometry (ICP-MS) suggests a stoichiometry of $Pt_{37}Au_{29}Cu_{34}$, that is close to Pt:Au:Cu = 1:1:1. In addition, X-ray diffraction (XRD) data (Fig. 5*C*) indicates minor phase segregation, but the predominant component is, indeed, PtAuCu. The lattice constant calculated from the XRD data is 0.388 nm, which is in agreement with the Vegard's-law–predicted value of 0.387 nm for the 1:1:1 Pt:Au:Cu stoichiometry. To test their HER activity, the as-synthesized PtAuCu nanoparticles were loaded onto carbon black (Cabot, Vulcan XC-72), and then thermally treated at 200 °C for 12 h to remove organic capping agents. The PtAuCu/C catalyst was tested for HER and compared with the commercial Pt/C catalyst (Fig. 5*D* and *SI Appendix*, Fig. S6 and Table S4). At an overpotential of 20 mV, the specific activity for the PtAuCu/C catalyst is 10.3 mA cm^{-2}, which is more than nine times that of Pt/C (1.08 mA cm^{-2}). The mass activity (η = 20 mV) for PtAuCu/C (3.33 A mg^{-1} Pt) is over seven times that of Pt/C (0.467 A mg^{-1} Pt). The HER performance of PtAuCu/C, in terms of mass activity, may be further improved by optimizing the particle size, composition, phase purity, and surface states, as well as by tuning local fine structure (e.g., core–shell). Finally, the PtAuCu/C catalyst was cycled 10,000 times with a negligible drop in activity, which suggests that this is also a long-lived catalyst (*SI Appendix*, Fig. S7).

Conclusions

In summary, we have introduced SPBCL combined with DFT calculations as a powerful platform for catalyst discovery, design, optimization, and synthesis. The focus of this work has been on HER catalysts, and we have used these techniques to identify a structure (1:1:1 PtAuCu alloy particles) that exhibits a mass activity seven times greater than a commercial Pt/C catalyst (based on Pt content). However, these techniques and observations, in principle, can be

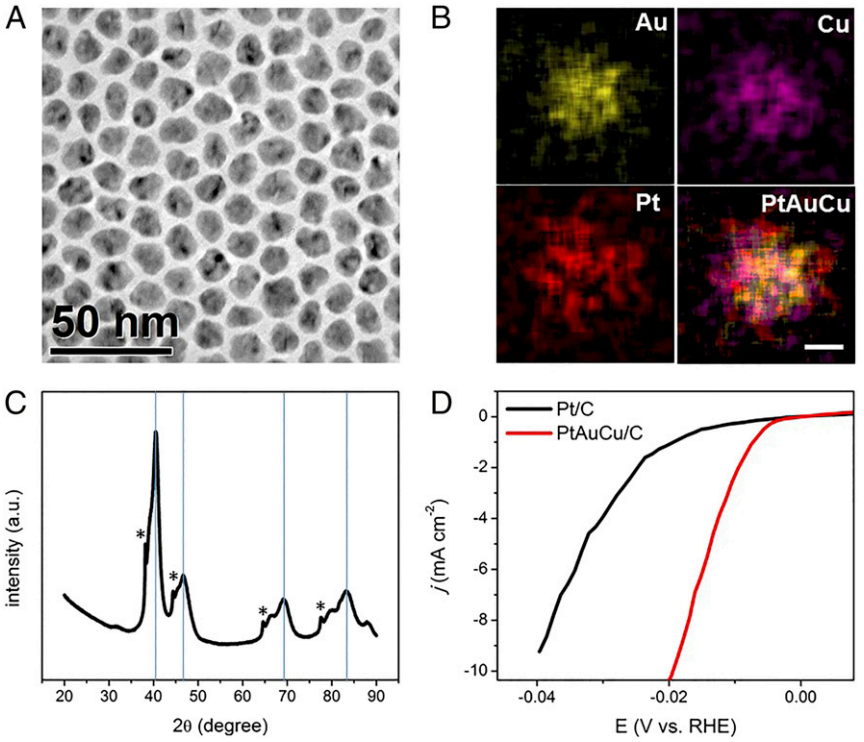

Fig. 5. (*A*) TEM image and (*B*) EDS maps of PtAuCu nanocatalyst. (*C*) XRD pattern of as-synthesized PtAuCu nanoparticles, in which the main component of PtAuCu is marked by the reference lines and the minor component of Au is marked by *. (*D*) HER polarization curves of PtAuCu/C and Pt/C. (Scale bar in *B*: 5 nm.)

extended to many other reactions, providing a means of discovering promising new catalyst structures as well as a method for refining them to achieve optimum performance. With recent developments in PPL technology (38), pen arrays with as many as 11 million tips enable large-scale fabrication of nanoparticle arrays with programmable specifications such as size, shape, and composition, providing a route to the high-throughput screening and discovery of new catalysts.

Experimental

Materials. Hexamethyldisilazane (HMDS) and hexane were obtained from Sigma-Aldrich. The block copolymer PEO-*b*-P2VP (Mn = 2.8-*b*-1.5 kg mol^{-1}, polydispersity index = 1.11) was purchased from Polymer Source. Metal precursors were purchased from Sigma-Aldrich. All of the above materials were used as received. Type M Dip-pen (DPN) arrays without gold coating were obtained from Nanoink. PPL arrays were acquired from TERA-print.

Ink Preparation. PEO-*b*-P2VP and metal compounds were dissolved in deionized water, and the solution was stirred for 2 d before use. The concentration of PEO-*b*-P2VP was 5 mg mL^{-1}. The pH of the solution was maintained between 3 and 4 by the addition of HNO_3.

DPN Patterning Process. For all DPN experiments, the DPN pen array was first dip-coated with the as-prepared block copolymer ink. After drying in air at room temperature, the pen array was loaded into a modified atomic force microscope (AFM) instrument (XE-150; Park Systems) in a chamber with controlled humidity at 95%. The array was placed in contact with a substrate to make predesigned arrays. Both TEM grids with silicon nitride and carbon support films were used as the substrate and were treated for hydrophobicity before use. They were placed in a desiccator with a small vial of an HMDS and hexane mixture (1:1, vol/vol) overnight.

PPL Patterning Process. PPL arrays were first treated with an oxygen plasma at 60 W for 5 min, followed by spin-coating the ink for 60 s at 11 × *g* with a ramping rate of 3 × *g*/s. After drying in air, the PPL arrays were placed into a modified AFM instrument (XE-150; Park Systems) and brought into contact with the substrate for patterning in a chamber with controlled humidity at 95%. Glassy carbon was spin-coated with HMDS for 60 s at 25 × *g* before use.

Thermal Treatment for Patterned Sample. After the patterning, the patterned substrate was transferred into a tube furnace for annealing. The treatment was programmed as follows: under Ar gas flow, ramp to 150 °C within 1 h, hold at 150 °C for 48 h, cool down to 25 °C within 1 h, switch the atmosphere to H_2, ramp to 500 °C within 2 h, hold at 500 °C for 12 h, cool down to 25 °C within 2 h.

Synthesis of PtAuCu Nanoparticles. A mixture of 0.2 mmol $Pt(acac)_2$, 0.2 mmol $HAuCl_4$, and 0.2 mmol $Cu(acac)_2$ was dissolved in 10 mL benzyl ether, 7.36 mL oleylamine, and 1.25 mL oleic acid under an Ar atmosphere. The reaction mixture was heated to 230–240 °C for 30 min. After reaction, the solution was cooled down and the products were isolated by adding ethanol and centrifugation. The nanoparticles were redispersed in hexane.

Electrochemical Measurements. The electrochemical measurements were performed in a three-electrode glass cell at 298 K using an Epsilon Eclipse Workstation or a Metrohm AutoLab equipped with a rotating-disk electrode. The patterned sample (or nanoparticles loaded on XC-72), Ag/AgCl electrode, and coiled platinum (or gold) wire were used as the working, reference, and counter electrode, respectively. The electrolyte was 0.5 M H_2SO_4 and was purged with Ar gas for 10 min before the measurements to remove dissolved O_2. Polarization data were collected by cyclic voltammetry at a scan rate of 5 mV/s (20 mV/s for PtAuCu/C). All potentials were calibrated versus a reversible hydrogen electrode.

Characterization. Optical images were taken with a Zeiss imager M2m. SEM images were taken with a Hitachi SU-8030 field-emission SEM at an acceleration voltage of 5 kV and a current of 15 μA. STEM images were taken with a Hitachi HD-2300 STEM at an acceleration voltage of 200 kV. The EDS spectra and mapping were obtained with a Thermo Scientific NSS 2.3. TEM images were taken with a Hitachi 8100 at an acceleration voltage of 200 kV. High-resolution TEM images were taken with a JEOL 2100F at an acceleration voltage of 200 kV. AFM measurements were performed on a Dimension Icon (Bruker) to obtain 3D profiles of the patterns. XRD spectra were collected on a Rigaku Ultima with a Cu Kα source. ICP-MS was collected on a Thermo iCAP Q mass spectrometer.

Computation. HBE calculations were based on DFT as implemented in the Vienna ab initio Simulation Package (VASP) using the projector-augmented

wave method (44–46). All calculations were performed with the revised Perdew–Burke–Ernzerhof exchange-correlation functional on periodically repeated metal slabs (47). A slab model with four atomic layers with a (3×2) unit cell and a vacuum region of 12 Å in thickness was used to calculate the HBEs on the (111) surfaces of pure metal (Ni, Pt, Cu, Au), bimetallic (Pt–Ni, Pt–Cu), and trimetallic (Pt–Cu–Au) systems. The bottom two layers were fixed and the top two layers were allowed to relax. An energy cutoff of 400 eV was used for the plane-wave basis set used to represent the electronic wave functions. Brillouin-zone integrations were sampled using Γ-centered *k*-point meshes corresponding to a $6 \times 10 \times 1$ grid. Spin polarization and dipole correction were included in all DFT calculations. The HBEs were calculated by $E_H = E_{H-\text{slab}} - E_{\text{slab}} - 1/2E_{H2(g)}$ where E_H is the binding energy of atomic hydrogen on the given slab, $E_{H-\text{slab}}$ is the total energy of the slab with 1/6 ML hydrogen adsorbed, E_{slab} is the total energy of the slab in vacuum, and $E_{H2(g)}$ is the energy of an isolated hydrogen molecule in the gas phase.

ACKNOWLEDGMENTS. This material is based, in part, upon work supported by GlaxoSmithKline LLC, Sherman Fairchild Foundation Inc., the Air Force Office of Scientific Research Award FA9550-16-1-0150, and the National Science Foundation Award DBI-1353682. P.G. gratefully acknowledges The Netherlands Organization for Scientific Research for the Rubicon Grant. M.L. gratefully acknowledges the support from the National Science Foundation (CBET-1264963). Y.K., X.F., and Y.Y. acknowledge the support from International Institute for Nanotechnology (IIN), Institute for Sustainability and Energy at Northwestern, National Natural Science Foundation of China, under Award 51601030, 21773023, and award of 1000-Talents Program (to Y.K.). This work made use of the Electron Probe Instrumentation Center (EPIC) facility of Northwestern University's Atomic and Nanoscale Characterization Experimental Center (NUANCE), which has received support from the Soft and Hybrid Nanotechnology Experimental (SHyNE) Resource (NSF ECCS-1542205); the Materials Research Science and Engineering Centers (MRSEC) program (NSF DMR-1121262) at the Materials Research Center; the IIN; the Keck Foundation; and the State of Illinois, through the IIN. This work made use of the J.B. Cohen X-Ray Diffraction Facility supported by MRSEC and SHyNE. This work made use of resources in National Energy Research Scientific Computing Center and Northwestern University's Quest high-performance computing system.

1. Reddington E, et al. (1998) Combinatorial electrochemistry: A highly parallel, optical screening method for discovery of better electrocatalysts. *Science* 280:1735–1737.
2. Li Y, Somorjai GA (2010) Nanoscale advances in catalysis and energy applications. *Nano Lett* 10:2289–2295.
3. Somorjai GA, Carrazza J (1986) Structure sensitivity of catalytic reactions. *Ind Eng Chem Fundam* 25:63–69.
4. Jacobs PW, Ribeiro FH, Somorjai GA, Wind SJ (1996) New model catalysts: Uniform platinum cluster arrays produced by electron beam lithography. *Catal Lett* 37: 131–136.
5. Habas SE, Lee H, Radmilovic V, Somorjai GA, Yang P (2007) Shaping binary metal nanocrystals through epitaxial seeded growth. *Nat Mater* 6:692–697.
6. Chen C, et al. (2014) Highly crystalline multimetallic nanoframes with three-dimensional electrocatalytic surfaces. *Science* 343:1339–1343.
7. Zuburtikudis L, Saltsburg H (1992) Linear metal nanostructures and size effects of supported metal catalysts. *Science* 258:1337–1339.
8. Somorjai GA (1996) Modern surface science and surface technologies: An introduction. *Chem Rev* 96:1223–1236.
9. Bell AT (2003) The impact of nanoscience on heterogeneous catalysis. *Science* 299: 1688–1691.
10. Burda C, Chen X, Narayanan R, El-Sayed MA (2005) Chemistry and properties of nanocrystals of different shapes. *Chem Rev* 105:1025–1102.
11. Lee H, et al. (2006) Morphological control of catalytically active platinum nanocrystals. *Angew Chem Int Ed Engl* 45:7824–7828.
12. Stamenkovic VR, et al. (2007) Improved oxygen reduction activity on $Pt_3Ni(111)$ via increased surface site availability. *Science* 315:493–497.
13. Herzing AA, Kiely CJ, Carley AF, Landon P, Hutchings GJ (2008) Identification of active gold nanoclusters on iron oxide supports for CO oxidation. *Science* 321:1331–1335.
14. Lee I, Delbecq F, Morales R, Albiter MA, Zaera F (2009) Tuning selectivity in catalysis by controlling particle shape. *Nat Mater* 8:132–138.
15. Peng Z, Yang H (2009) Designer platinum nanoparticles: Control of shape, composition in alloy, nanostructure and electrocatalytic property. *Nano Today* 4:143–164.
16. Kang Y, et al. (2013) Heterogeneous catalysts need not be so "heterogeneous": monodisperse Pt nanocrystals by combining shape-controlled synthesis and purification by colloidal recrystallization. *J Am Chem Soc* 135:2741–2747.
17. Wang C, et al. (2009) Monodisperse Pt_3Co nanoparticles as a catalyst for the oxygen reduction reaction: Size-dependent activity. *J Phys Chem C* 113:19365–19368.
18. Zhang L, et al. (2015) Platinum-based nanocages with subnanometer-thick walls and well-defined, controllable facets. *Science* 349:412–416.
19. Tian N, Zhou ZY, Sun SG, Ding Y, Wang ZL (2007) Synthesis of tetrahexahedral platinum nanocrystals with high-index facets and high electro-oxidation activity. *Science* 316:732–735.
20. Bu L, et al. (2016) Biaxially strained PtPb/Pt core/shell nanoplate boosts oxygen reduction catalysis. *Science* 354:1410–1414.
21. Si R, Flytzani-Stephanopoulos M (2008) Shape and crystal-plane effects of nanoscale ceria on the activity of Au-CeO_2 catalysts for the water-gas shift reaction. *Angew Chem Int Ed Engl* 47:2884–2887.
22. Greeley J, Jaramillo TF, Bonde J, Chorkendorff IB, Nørskov JK (2006) Computational high-throughput screening of electrocatalytic materials for hydrogen evolution. *Nat Mater* 5:909–913.
23. McCrory CCL, et al. (2015) Benchmarking hydrogen evolving reaction and oxygen evolving reaction electrocatalysts for solar water splitting devices. *J Am Chem Soc* 137:4347–4357.
24. Chu S, Majumdar A (2012) Opportunities and challenges for a sustainable energy future. *Nature* 488:294–303.
25. Turner JA (2004) Sustainable hydrogen production. *Science* 305:972–974.
26. Sheng W, et al. (2015) Correlating hydrogen oxidation and evolution activity on platinum at different pH with measured hydrogen binding energy. *Nat Commun* 6: 5848.
27. Kitchin JR, Nørskov JK, Barteau MA, Chen JG (2004) Modification of the surface electronic and chemical properties of Pt(111) by subsurface 3d transition metals. *J Chem Phys* 120:10240–10246.
28. Stamenkovic V, et al. (2006) Changing the activity of electrocatalysts for oxygen reduction by tuning the surface electronic structure. *Angew Chem Int Ed Engl* 45: 2897–2901.
29. Nørskov JK, Bligaard T, Rossmeisl J, Christensen CH (2009) Towards the computational design of solid catalysts. *Nat Chem* 1:37–46.
30. Lv H, et al. (2015) A new core/shell NiAu/Au nanoparticle catalyst with Pt-like activity for hydrogen evolution reaction. *J Am Chem Soc* 137:5859–5862.
31. Lu Q, et al. (2015) Highly porous non-precious bimetallic electrocatalysts for efficient hydrogen evolution. *Nat Commun* 6:6567.
32. Zhang J, Sasaki K, Sutter E, Adzic RR (2007) Stabilization of platinum oxygen-reduction electrocatalysts using gold clusters. *Science* 315:220–222.
33. Kang Y, et al. (2014) Multimetallic core/interlayer/shell nanostructures as advanced electrocatalysts. *Nano Lett* 14:6361–6367.
34. Wang C, et al. (2011) Multimetallic Au/$FePt_3$ nanoparticles as highly durable electrocatalyst. *Nano Lett* 11:919–926.
35. Chai J, et al. (2010) Scanning probe block copolymer lithography. *Proc Natl Acad Sci USA* 107:20202–20206.
36. Chen P-C, et al. (2015) Tip-directed synthesis of multimetallic nanoparticles. *J Am Chem Soc* 137:9167–9173.
37. Chen P-C, et al. (2016) Polyelemental nanoparticle libraries. *Science* 352:1565–1569.
38. Huo F, et al. (2008) Polymer pen lithography. *Science* 321:1658–1660.
39. Subbaraman R, et al. (2011) Enhancing hydrogen evolution activity in water splitting by tailoring Li^+-$Ni(OH)_2$-Pt interfaces. *Science* 334:1256–1260.
40. Ruban AV, Skriver HL, Nørskov JK (1999) Surface segregation energies in transition-metal alloys. *Phys Rev B* 59:15990–16000.
41. Chen W, Schmidt D, Schneider WF, Wolverton C (2011) Ordering and oxygen adsorption in Au- Pt/Pt(111) surface alloys. *J Phys Chem C* 115:17915–17924.
42. Murray CB, Kagan CR, Bawendi MG (2000) Synthesis and characterization of monodisperse nanocrystals and close-packed nanocrystal assemblies. *Annu Rev Mater Sci* 30:545–610.
43. Sheng W, Myint M, Chen JG, Yan Y (2013) Correlating the hydrogen evolution reaction activity in alkaline electrolytes with the hydrogen binding energy on monometallic surfaces. *Energy Environ Sci* 6:1509–1512.
44. Kresse G, Furthmüller J (1996) Efficient iterative schemes for ab initio total-energy calculations using a plane-wave basis set. *Phys Rev B Condens Matter* 54:11169–11186.
45. Kresse G, Furthmüller J (1996) Efficiency of ab-initio total energy calculations for metals and semiconductors using a plane-wave basis set. *Comput Mater Sci* 6:15–50.
46. Kresse G, Joubert D (1999) From ultrasoft pseudopotentials to the projector augmented-wave method. *Phys Rev B* 59:1758–1775.
47. Hammer B, Hansen LB, Nørskov JK (1999) Improved adsorption energetics within density-functional theory using revised Perdew-Burke-Ernzerhof functionals. *Phys Rev B* 59:7413–7421.
48. Denton AR, Ashcroft NW (1991) Vegard's law. *Phys Rev A* 43:3161–3164.
49. Wang C, Markovic NM, Stamenkovic VR (2012) Advanced platinum alloy electrocatalysts for the oxygen reduction reaction. *ACS Catal* 2:891–898.